Advances in Knowledge-Based Systems, Data Science, and Cybersecurity Received 10-10-2024; Accepted 14-12-2024; Published 21-12-2024

Integrated Artificial Intelligence Approach for Diabetic Foot Ulcer Assessment: A Comprehensive Solution for Precision Diagnosis and Patient Care

Karam Hussein Jasim Al-Bahar karamhussein191@gmail.com
Technical Engineering College of Mosul, Northern Technical University (NTU)
Mosul, Iraq

Younus Jasim Taha Al- Taha yssjss010@gmail.com
Technical Engineering College of Mosul, Northern Technical University (NTU)
Mosul, Iraq

Marwa Mawfaq Mohamedsheet Al-Hatab marwa.alhatab@ntu.edu.iq
Technical Engineering College of Mosul, Northern Technical University (NTU)
Mosul, Iraq

Ahmed S. Ibrahim Al-Obaidi ahmedsaeed@ntu.edu.iq
Technical Engineering College of Mosul, Northern Technical University (NTU)
Mosul, Iraq

Corresponding Author: Marwa Mawfaq Mohamedsheet Al-Hatab

Abstract

Diabetic Foot Ulcers (DFUs) pose significant healthcare challenges, often resulting in severe complications and amputations. A prompt as well as precise evaluation of extent of wound must be performed for successful treatment and enhanced results for patients. The study offers novel method for automatically identifying vascular problems with diabetic foot by employing infrared thermography. The study employs a dataset comprising 710 thermal images acquired from Al_Wafa Specialized Center for Diabetes and Endocrinology and Bartella General Hospital, which has been meticulously curated for research purposes. To address specific challenges encountered in diabetic foot imaging and diagnosis, have been introduced three tailored CNN (Convolutional Neural Network) architectures, each designed to identify different risk levels associated with diabetic foot complications. Low-level Diabetic Foot Infection Network (LL-DFI-Net): This architecture is aimed at the detection of low-risk groups, Medium-Level Diabetic Foot Infection Network (ML-DFI-Net) Designed for the medium-risk group, this model targets neuropathic individuals who do not exhibit signs of ischemia. High-Level Diabetic Foot Infection Network (HL-DFI-Net): Focused on high-risk group, this architecture is specialized for detecting individuals with ischemia. The three networks have achieved high accuracy, as follows: LL-DFI-Net achieved 96.7213%, ML-DFI-Net recorded 97.916%, HL-DFI- reached 100%. These models aim to improve identification and treatment of diabetic foot conditions, improving healthcare strategies as well as patient results.

Citation: Karam Hussein Jasim Al-Bahar et al. Integrated Artificial Intelligence Approach for Diabetic Foot Ulcer Assessment: A Comprehensive Solution for Precision Diagnosis and Patient Care. Advances in Knowledge-Based Systems, Data Science, and Cybersecurity. Research 2024;1(1):4. Pages: 61-77

Keywords: Thermal Images, Diabetic Foot Ulcers (DFUs), Convolutional Neural Network (CNN), and Deep Learning (DL)

1. INTRODUCTION

One of most important areas of medical study involves application of thermal imaging to identify DF (diabetic foot). With the projected rise in the number of diabetic patients to 439 million by 2030 from 194 million in 2004, there is a pressing need for effective measures to address this issue. Foot complications are a significant risk factor for diabetes, particularly in its later stages. Diabetic foot ulcers are a prevalent complication that, if left untreated, can result in partial or complete amputation. Detecting and treating DF ulcers early can mitigate these consequences. However, traditional diagnostic methods are often inadequate for early detection, as they pose challenges for patients with neuropathy to self-examine and lack automation[1].

Existing research has demonstrated a clear connection between higher temperatures and the development of DF ulcers. In order to detect these ulcers at an early stage, multiple algorithms have been put forth, including the utilization of infrared images [2–6], liquid crystal thermography (LCT) [7], infrared (IR) thermometers, and temperature sensors incorporated into weighing devices[8].

This study introduces a novel application of infrared thermography combined with tailored CNN architectures for the assessment of diabetic foot ulcers. Unlike existing methodologies, our approach focuses on distinguishing different risk levels of foot complications using specialized models each optimized for detecting varying degrees of vascular disorders in diabetic patients. These models employ unique computational techniques that enhance detection accuracy and provide a more comprehensive solution for precision diagnosis. Specifically, we introduce three distinct CNN architectures tailored for this task:

1. Low-Level Diabetic Foot Infection Assessment Network (LL-DFI-Net) - for the first level.
2. Medium-Level Diabetic Foot Infection Assessment Network (ML-DFI-Net) - for the second level.
3. High-Level Diabetic Foot Infection Assessment Network (HL-DFI-Net) - for the third advanced high level. Each architecture is designed to address specific challenges encountered in diabetic foot imaging and diagnosis.
   - (HL-DFI-Net) specializes in fine-grained analysis of foot regions captured through infrared thermography, extracting intricate features indicative of vascular abnormalities for group K2: high-risk group.
   - (ML-DFI-Net) focuses on robust detection of vascular patterns and anomalies present in infrared thermography images. for group K1: Meduim-risk group.
   - (LL-DFI-Net) extends traditional CNN architectures by incorporating domain-specific knowledge and clinical insights relevant to diabetic foot pathology for group K0: Low-risk group.

All patient data used in this study were anonymized to protect privacy, following strict ethical guidelines approved by the institutional review boards of Al-Wafa Specialized Center for Diabetes and Endocrinology and Bartella General Hospital. The thermal images were stripped of any identifying information before analysis, and access to the dataset was restricted to authorized personnel only

The remainder of this article was structured offering thorough insight into our research and findings. Section 2 reviews existing studies on the use of thermal images for DF detection. Section 3 describes materials and methods, including the specifics of thermal imaging data collection from the Al-Wafa Specialized Center for Diabetes and Endocrinology. Section 4 delves into the details of our proposed CNN architectures and their implementation. Also results of our simulations are analyzed and discussed

2. LITERATURE REVIEW

Review of literature Direct temperature measurement is not possible via remote temperature measurement methods. Rather, they measure body's energy flow and utilize this information to calculate temperature (radiometry). The foundation of radiation measurement depends on observation that all objects, having temperatures greater than 0 Kelvin, generate electromagnetic radiation in variety of wavelengths. Thermal infrared, or (IR), is term employed to describe majority of radiation from nearby objects, such as those with temperatures between $0 - 100°$Celsius, that have wavelengths of 3mm or longer. For instance, at 300 K (27°Celsius), an object's peak radiation was 9µm. In the visible spectrum, objects in this temperature range don't produce any discernible radiation. Only items heated to 500°C or higher—such as red hot metal—emit detectable radiation in the visible spectrum [2]. The scientist Gasim employed remote thermometers (pyrometers) in 2013, while there have been other approaches based on plantar temperature distributions. Effective as well as dependable measurements include temporal artery thermometry along with tympanic membrane temperature. Similar to core body temperature, telethermometers were frequently employed in wound care to record ambient as well as wound temperatures [3]. The two scientists, Swati Madhi and Bali Mahajan, in 2014. introducing this research, which includes the most recent image processing methods for thermogram-based nontraumatic thyroid illness detection. A technique called thermal imaging uses heat emitted from an item to produce analytical images. We have suggested a method that uses thermal imaging to identify thyroid illness. Since an overactive thyroid gland has become site of elevated chemical activity as well as blood flow, thermal sensors can identify it as source of heat production. The FLIR-E30 thermal camera has thermal sensitivity of 0.1°C and can detect temperatures between $-°$C and 120°C [4]. Scientist Capo employed thermal imaging in 2015 to track how well psoriasis patients were responding to therapy since leveling of temperature gradients has been linked to both joint effect as well as disease recovery [5]. According to a 2016 research carried out scientist Fryberg and colleagues, a smart heated foot pad may be able to identify inflammation five weeks before they become clinically noticeable. Studies in this field fill a significant vacuum in existing literature since these reports were less frequent than those of single patients [6]. An alteration in the distribution of temperatures prior to and following endovascular therapy or surgical bypass was seen by authors of at least one research (Lin & Saines, 2017) involving 8patients who had lower extremity occlusive disease. Arterial duplex ultrasonography confirmed the increased flow. Blood flow can be imaged and assessed using thermal image time series. Temporal temperature changes can be employed in these methods to assess a number of physiological processes, such as vasomotion.

The signals in the following five frequency bands have different origins: endothelium (metabolic), neuronal, muscular, respiratory, and cardiac. These are 0.005-0.02 Hz,0.02-0.05 Hz,0.05-0.15 Hz,0.15-0.4 Hz, as well as 0.4-2.0 Hz. All of findings point to the effectiveness of thermal imaging in determining skin's perfusion in both diabetic patients as well as healthy individuals [7]. Raghav, a scientist, presented a study on diabetic foot ulcers (DFU) in 2018. It is among the most significant side effects of diabetes. According to estimates, 4–10% of people have diabetes each year, and those who have disease having 15 - 25 percent lifetime risk of getting these ulcers. Lower limb amputation constitutes a single of the most debilitating effects of diabetes, which foot ulcers exacerbate. A DFU might get infected and need complete or partial amputation of affected limb if no medications are obtained. Diabetic ulcers were reason behind nearly 50 percent of non-traumatic lower limb amputations. In 2018, Raghav et al. [9]. In a 2019 study of 277 diabetic individuals, researcher Astacio Picado et al. discovered that temperatures significantly lower beneath 1^{st} metatarsal head, 5^{th} metatarsal head, heel, and big toe core of left foot. It is the same with patients. In order to assess cutaneous blood perfusion in vasculopathy, neuropathy, as well as vascular neuropathy groups, authors contrasted laser Doppler flowmetry, laser Doppler imaging, and thermography with non-neuropathy group. They discovered that in seven healthy adults, thermography and laser Doppler imaging had a correlation of $r = 0.577$ ($p < 0.01$, $n = 38$). Additionally, they discovered that laser Doppler imaging as well as infrared thermography were correlated with $r = 0.358$ ($p < 0.01$, $n = 60$) in 10 scleroderma patients.[10]. The body's ability to constrict blood vessels in skin regions exposed to cold temperatures (apart from face, neck, and chest) in order to stop heat loss was investigated by scientist Lim in 2020. Perhaps hand responds to body's thermoregulatory demands more actively than any other portion of the body. The fingertips of hand get most heat when temperature rises, and vessels throughout hand dilate. Cooling causes this tendency to reverse. The hand's blood vessels contract, resulting in an 8-degree Celsius variation in skin temperature. A cold hand reduces amount of body heat it transfers to the surroundings. So, even though temperature although upper body is largely unchanged, an infrared image obtained a few minutes after the body has gone from Warm surroundings (30°Celsius) to somewhat chilly environment (22.6°Celsius) reveals that blood vessels in hand were already well constricted[11]. 70 patients in intensive care unit participated in blinded, prospective cohort trial that had been carried out in 2021 by researchers Siman and Angel. Using thermal imager, participants' bilateral sacrum and heel region were examined. Following patient's admission and at 3, 7, 14, & 25 days, follow-up imaging had been completed. The thermal images were not visible to doctors, and all subjects received routine wound care and prophylaxis. Evaluating thermography to identify physiological changes that may precede visual changes and not be evident in deep tissue injury (DTI), reducing subjectivity along with complexity of visual evaluation, and assessing economical effect of using thermal imaging technology were the goals[12]. Kay et al. conducted an evaluation of 415 ICU patients who were included through convenience sampling in 2022. The Utilizing Braden scale, possibility of PI (pressure injury), and infrared thermal imager was used once a day for ten days to acquire thermal images of sacral region. Ideal skin cutoff value 6 temperatures to forecast pressure injuries has been recognized by comparing prediction impacts of infrared thermography as well as Braden scale on PI using a receiver operating characteristic curve. The researchers discovered a negative correlation between the risk of PI and the sacral region's relative temperature [13].

3. RESEARCH METHODOLOGY

3.1 Dataset Description

Dataset employed within study comprises 710 thermal images obtained from Al-Wafa Specialized Center for Diabetes and Endocrinology and Bartella General Hospital, meticulously curated for research purposes. The dataset is structured into distinct folders representing different health conditions. In the Diabetic Group, three risk categories are delineated: K0 denotes the Low-risk group, encompassing non-neuropathic and non-ischemic individuals; K1 designates the Medium-risk group, consisting of neuropathic individuals without ischemia; and K2 represents the High-risk group, which includes individuals with ischemia. Each subgroup (K0, K1, and K2) contains thermal images captured at two time points, denoted as T0 and T10, corresponding to acquisitions before and after utilization of cold stress test, respectively. For instance, the image K0-0001 corresponds to the acquisition at T0 for a patient, while K0-0002 corresponds to the acquisition at T10 for the same patient. In the Healthy Group, participants who did not undergo the cold stress test are represented by images M-0001 to M-0039, whereas control subjects who underwent the test are represented by images M-0040 to M-0125. This meticulous organization facilitates a comprehensive analysis of thermal imaging data within distinct health conditions and stress test scenarios. Preprocessing data : involved the conversion of the 710 images across the four groups from RGB to grayscale, followed by resizing to dimensions of 256x256. While the dataset used in this study comprises 710 thermal images, we recognize that this sample size may limit how broadly applicable our findings. Upcoming work will concentrate on expanding dataset by collaborating with additional medical centers and incorporating data from diverse populations. Additionally, we aim to perform external validation of our models using larger, independent datasets to further assess their robustness.

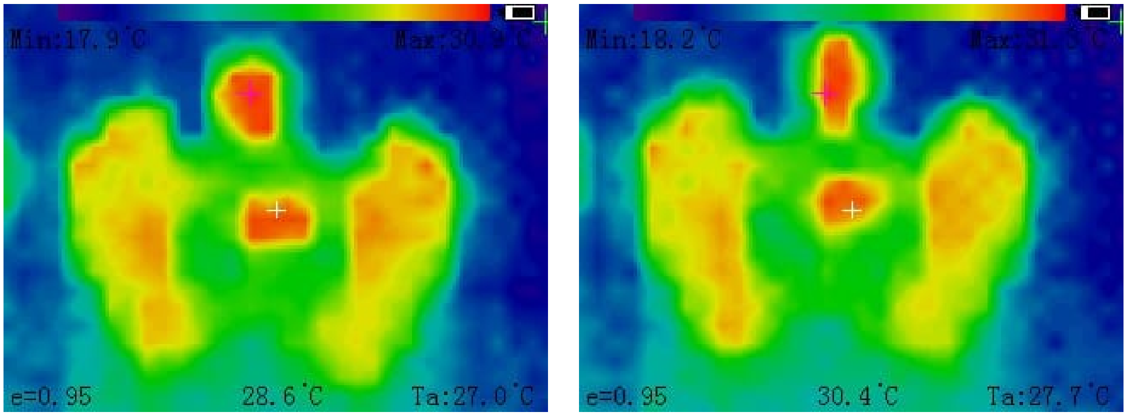

(a) (b)

Figure 1: the sample of data used in this study for normal (a)and abnormal(b) case

3.2 Classification Models

In this investigation, the focus is on the critical task of classifying diabetic foot diseases through the analysis of thermal images. This is pursued for two primary reasons: firstly, to address conditions that significantly impact daily lives and well-being of individuals, and secondly, to explore the categorization of key symptoms that manifest across various stages of diabetic foot conditions. This study begins with the analysis of thermal imagery for determining inflammation as well as other related symptoms indicative of DF diseases. Progressing further, attention is given to areas exhibiting temperature variations, which correlate to different disease states, moving from early-stage signs detectable in the lower extremities to more advanced conditions. Finally, the study extends to a comprehensive evaluation of thermal patterns associated with severe diabetic foot complications[14].

This study differentiates itself by introducing tailored CNN architectures specifically designed to address the varying risk levels in diabetic foot ulcer detection. A detailed comparison with existing state-of-the-art methods is provided, showing how our approach achieves higher accuracy and better adaptability to different patient conditions. Furthermore, novelty of suggested model is found in its capacity to integrate infrared thermography data, which is underutilized in current diagnostic practices., and applied to yield high classification accuracies as illustrate in FIGURE 2. This project encompasses several logical phases. Initially, thermal images depicting various stages of diabetic foot diseases are gathered, with a detailed consideration of orthogonal patterns representing temperature variations across different areas of the foot.

Subsequent to the image collection, pre-processing steps such as normalization and cropping are applied to the images to ensure consistency. Feature extraction from the thermal images was conducted using advanced preprocessing techniques, converting RGB images to grayscale, resizing, and applying specialized filters to enhance relevant features. The CNN architectures then automatically identified key thermal patterns associated with different risk levels. These features were further analyzed to correlate with known clinical markers, providing a more detailed understanding of how the models differentiate between risk categories.

Moreover, the thermal images were segregated into 2 groups for training as well as testing phases of classification models, setting the stage for an in-depth analysis and understanding of diabetic foot diseases. Consequently, DL models are designed as (LL-DFI-Net) , (ML-DFI-Net) and (HL-DFI-Net). Basically, trained image set was employed to train all network models, and tested image set was utilized to test same networks. Additionally, convolution, ReLU, and pooling layer DL settings are assessed to determine how to get best accuracies [15].

The three suggested models are grounded in CNN architecture, each tailored to process a unique aspect of diabetic foot disease imagery. These models are characterized by the integration of various evaluated parameters across numerous layers, enabling the effective classification of specific diabetic foot conditions. The architecture of each model is straightforward yet powerful, incorporating fundamental layers of input, Rectified Linear Unit (ReLU), convolution, FC (fully connected), pooling, softmax, as well as output layers, as illustrated in FIGURE 3. The details and parameters of each layer, which are pivotal for the models' functionality, will be elaborated in the subsequent sections[16].

- **The initial layer** in analysis of diabetic foot disease imagery handles grayscale images. It captures pixel intensity values based on the image's resolution and size. In this examination, grayscale images are utilized, each defined by a matrix of dimensions (width × height × 1), where ”1” signifies a single channel that represents grayscale intensity. Unlike colored images

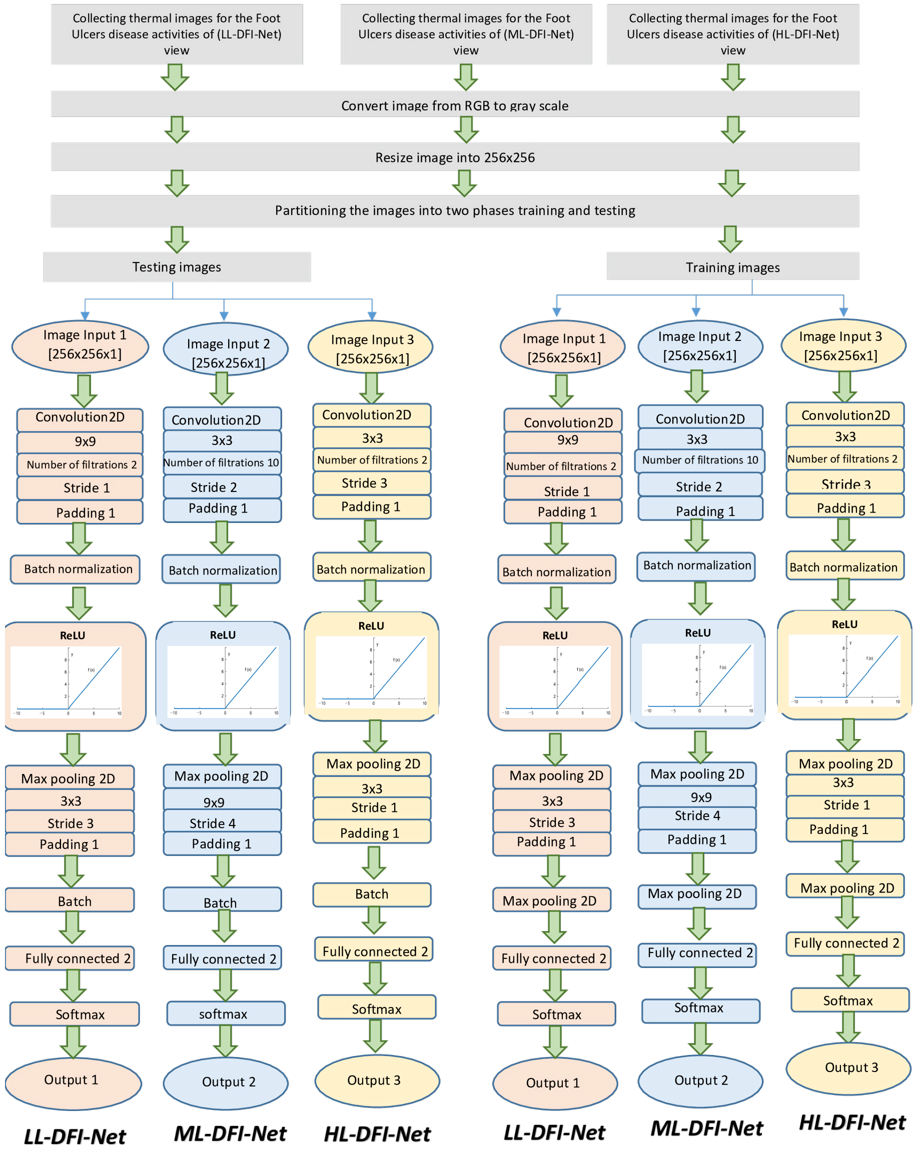

Figure 2: shows the most important stages of three networks LL-DFI-Net, ML-DFI-Net and HL-DFI-Net.

that necessitate 3 channels for RGB (Red, Green, & Blue), grayscale images simplify process by focusing on variations in lightness or darkness. The dimensions, width as well as height, were customized for every individual model to meet necessary perspectives of ((LL-DFI-Net) , (ML-DFI-Net) and (HL-DFI-Net)). The single grayscale channel is subsequently processed in layer that follows, known as convolution layer[17].

- **In the convolution layer**, the grayscale image undergoes processing through multiple filters or kernels. Each kernel, acting as a unique set of weights, convolves image's single channel. This convolution, performed across various kernels, generates multiple feature maps, each

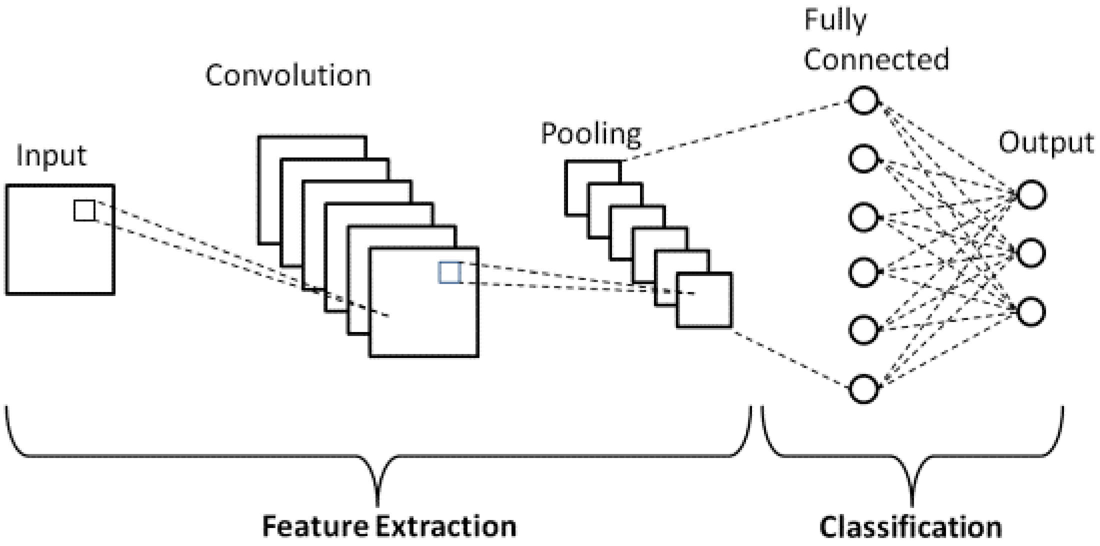

Figure 3: A general CNN architecture for image classification task

highlighting different aspects of the image's texture, edges, or other relevant features for identifying characteristics of diabetic foot diseases. The procedure entails breaking the channel up into smaller parts as well as applying the convolution operation, which is mathematically defined by a specific formula that takes into account the convolution kernel's dimensions, the pixel positions, and the kernel weights. The resulting image channels are called feature maps. Here is the formula employed to calculate the feature map values [18]:

$$\mathrm{Au, v, c^{l} = Uc^{l}} + \sum_{\mathrm{i=-H_{h}^{I}}}^{\mathrm{H_{h}^{I}}} \sum_{\mathrm{j=-H_{w}^{I}}}^{\mathrm{H_{w}^{I}}} \sum_{\mathrm{I-1=1}}^{\mathrm{c^{I-1}}} \mathrm{w}^{\mathrm{c^{I}}}_{\mathrm{i+H^{I}}_{\mathrm{W,j,H^{I}_{W},C^{I-1}F}_{\mathrm{u+i+j,c^{I-1}}}}} \tag{1}$$

where: Au,v,c l represents output of convolution layer, (u,v) denotes pixel coordinate, Uc l represents channel bias, $Wi, j, c\ l - 1\ c\ l$ denotes kernel weighs, c represents channel number, $Hw\ l$ were respectively width & height of convolution layer kernel, $Hh\ l$ denotes current layer, and $l - 1$ represents previously layer.

In context of digital image processing, utilizing fixed kernel values enables selective filtering of image channels. By applying diverse kernels to each channel, a variety of feature maps can be generated, offering multiple perspectives of filtering analysis for individual channel images. The convolution process leverages several parameters encompassing filter's dimensions, padding, quantity, as well as stride to manipulate images [19].

Within deep learning (DL) networks, particularly in CNNs, ReLU (Rectified Linear Unit) stands as predominant activation function. Primary objective was to cause the network to become nonlinear by allowing passage of positive values or zero, effectively determining activation state of a neural network neuron [20]. This is achieved by retaining positive inputs as is and converting any negative input to zero, thereby simplifying the computational complexity and enhancing model's performance. It can be stated as:

$$\mathrm{Mu, v, c^{I}} = \max\left(0, \mathrm{A^{I}_{u,v,c}}\right) \tag{2}$$

where: Mu,v,c l represents output of ReLU, max denotes maximum operation, as well as Au,v,c l represents input positive value to ReLU activation function [20].

Information was down-sampled through pooling. The spatial dimensions are capable of further reduced by this layer, but depth cannot. In particular, it comes after the nonlinearity of ReLU, which comes after the convolution processes. It generates a fresh set of feature maps by working with each one independently. Pooling operation's size has to be less than that of feature map. According to FIGURE 3, this leads to reduction in amount of pixels in each prior feature map. Therefore, by lowering the model's overfitting, the pooling layer might aid in reducing size of feature maps therefore enhancing efficiency [21]. There are 2 popular kinds of pooling:

- Maximum Pooling (MP): It determines highest values of the windows, or tiny matrices, in every feature map that has come before it. This equation governs application of MP operation:

$$\mathrm{Pa^{1}, b^{1}, cMax} = \underset{0\le a<ph, 0\le Pw}{\mathrm{MAX}} \mathrm{M_{a^{1}xph+a, b^{1}xP_{W}+B,C}} \tag{3}$$

Here: $\mathrm{Pa^{1}, b^{1}, cMaxi}$ represents output of pooling layer of maximum type, 0 ≤ al < phI, phI denotes height of pooled channel, 0 ≤ bl < pwl, pw represents width pooled channel, 0 ≤ c < cl = cl -1, ph denotes height of each pooled window and pw represents width of each pooled window.

- Average Pooling (AP): It determines average values of each feature map's tiny matrices (windows). The AP procedure can be utilized via equation below:

$$\mathrm{J_{ave}}(\mathrm{M}) = \frac{1}{\mathrm{SXS}} \sum_{\mathrm{i}=1}^{\mathrm{S}} \mathrm{M_i} \tag{4}$$

  where: Jave represents output of pooling layer of average type, S denotes pooling region size as well as Mi was output ReLU.

  - **The fully connected (FC) layer** was designed to create connections between each node in layer and each node in the one below. This architecture facilitates transition between feature extraction phase as well as classification phase within DL model. By transforming feature maps into a flattened vector, the FC layer serves as initial layer in classification segment. Output from this layer is determined based according to following equation:

$$\mathrm{G_r} = \sum_{\mathrm{a}=1}^{\mathrm{n_1^{I-1}}} \sum_{\mathrm{b}=1}^{\mathrm{n_2^{I-1}}} \sum_{\mathrm{c}=1}^{\mathrm{n_3^{I-1}}} \mathrm{U^{I}_{a,b,c,r}} \left(\mathrm{P_S}\right)_{\mathrm{a,b}} \qquad \forall 1 \le \mathrm{r} \le \mathrm{n1} \tag{5}$$

where: FC layer's output represents G, width of previous pooling channel constitutes $n1\ l-1$, height of previous pooling channel represents $n2\ l-1$, number of previous pooling channels is $n3\ l-1$, pooling layer output is (Ps)a, b, weight between pooling alongside FC layers was $Ua, b, c, r\ l$, as well as necessary number of classes represents n l.

Typically positioned before final classification layer,

- the softmax layer had been utilized to calculate probability distribution across various output classes for a given input. This process ensures that the output values are proportionally distributed, representing likelihood of each class. However, as number of classes grows, computational cost associated with softmax layer can increase significantly. The equation that follows represents softmax function formula:

$$\mathrm{X_r} = \frac{\exp(\mathrm{G_r})}{\sum_{\mathrm{s=1}}^{\mathrm{n^{I-1}}} \exp(\mathrm{G_s})} \tag{6}$$

here: X*r* signifies softmax layer's output. Stated differently, softmax function normalizes each node's output values to fall between 0 - 1. Each output's value is divided by the sum of values of all other outputs.

- Final layer in sequence was **classification layer**, which allocates incoming input to most appropriate category. It is responsible for generating final decision output. The functioning of this layer is governed by a principle reffered as ”winner-takes-all” . The following describes how this layer functions:

$$\mathrm{D_r} = \begin{cases} 1 & \text{if } \mathrm{y_{r=max}} \\ 0 & otherwise \end{cases} \tag{7}$$

Here, max represents extracted maximum *yr* value and *Dr* denotes output choice of classification layer. Final layer was tailored to differentiate among various aspects of diabetic foot disease based on specific characteristics. This approach is uniformly applied across all models, including (LL-DFI-Net), (ML-DFI-Net), and (HL-DFI-Net). Such a pattern suggests that this research has notably achieved success in accurately identifying different manifestations of diabetic foot disease across each axis.

4. RESULTS AND DISCUSSIONS

4.1 Established Dataset

Diabetic Foot Ulcers (DFUs) dataset was employed as first data set for trials. A large number of thermal images for detection of vascular disorders in diabetic feet utilizing infrared thermography have been collected for the three case of DFUs, low, medium and high.

Total 710 thermal images acquired from Al_Wafa Specialized Center for Diabetes and Endocrinology and Bartella General Hospital. This image divided into three group, everyone has normal and abnormal case: Low-level Diabetic Foot Infection have 150 normal image with 120 otherwise, Medium-level Diabetic Foot Infection have 120 normal with 80 abnormal and High-level Diabetic Foot Infection having the same number 120 image.

Images were taken from October 6, 2023, until February 9, 2024. A thermal imager infrared camera has sensor (MLX90640ESF-BAB) is used [22], with featuring a 2.8-inch screen boasting a resolution of 320x240, it offers a continuous usage of up to 4 hours, even during charging. Offering a temperature measurement range from −40°C to +300°C, along with an 8Hz. it captures images with standard dimensions $320 \times 240 \times 3$ pixels as well as JPG format. The field of view is 55° horizontally and 35° vertically The distance between camera and patient's organ is 1 meter.

4.2 Standardizations

Each investigation will be conducted using a laptop computer with specifications listed below: Lenovo brand, 8 GB of computer memory, GF117 graphics processor, Intel Core i5 processor running at 2.50 GHz, NVIDIA external graphics card, alongside 2 GB of display memory. ASA collection contains 710 photos in total, with 34 images utilized for each letter of Arabic alphabet. Additionally, every trial is taken into account for following training parameters: a fixed learning rate of 0.0001, an optimizer type of SGDM (Stochastic Gradient Descent with Momentum), a momentum value 0.9, & weight decay value 0.0001. maximum epochs of 20 and mini-batch size of 128. Three groups have been randomly selected from the DFU dataset: 50 percent will be used for training (following [23–26]), 25 percent will be used for testing, and 25 percent will be used for validation. As will be explained later, the gathered input photos have been empirically downsized to $256 \times 256 \times 1$ pixels. This work is divided in to three cases: Low-level Diabetic Foot Infection, Medium-level Diabetic Foot Infection and High-level Diabetic Foot Infection. The number of output class for each case is fixed to the 2, where each one of them refers to the normality or abnormality for these problem.

4.3 Data Parameters

The appropriate parameters of the suggested DFI network have been investigated through extensive experiments. This paper working for three cases for disease DFI, low level, mid. And high of Diabetic Foot Infection. Its parameters are tuned and distributed into eight stages for every case, where just one parameter changes significantly at time. The low-level results of the comprehensive experiments conducted to determine the proper parameters of the proposed Diabetic Foot Infection Network (DFI-Net) for the established DFU dataset are displayed in TABLE 1, while the other case process is shown in the same table with parameters that differ.

Two fundamental layers—convolution alongside pooling layers—are where parameters that need to be evaluated are divided. Stride Size, Filter size, number of filters, as well as zero padding size are controllable by the convolution layer. Pooling layer settings include stride size, window size, type, as well as zero padding size. The studies were separated into 8 phases, each of which focuses on altering a particular parameter's value while maintaining values of other parameters. Up to stage 8, where it's possible to benchmark best %age, best accuracy is always noted and monitored for use in the following step.

The filter size is progressively increased for the convolution layer from 3x3 pixels to 13×13 pixels. 9×9 pixels have the highest precision, 93.44%, on record. When the number of filters is adjusted between two and fourteen, two filters are discovered to be the optimal quantity in order to maintain the highest result from the past. The stride size can be adjusted between 1x1 and 5 pixels; 1x1 pixels have been shown to perform the best, with a 93.44% rate. When 0 padding size was changed from 0

Table 1: The performances of extensive experiments that are implemented to obtain the appropriate parameters of the proposed LL-DFI network for the established DFU dataset

Cases	Conv.				Pooling				Accuracy (%)
	Filter size	No. of filters	Stride	Padding	Type	Size	Stride	Padding	
1	3 × 3	2	1	1	Max	3 × 3	1	1	90.72
	5 × 5	2	1	1	Max	3 × 3	1	1	89.08
	7 × 7	2	1	1	Max	3 × 3	1	1	91.44
	9 × 9	2	1	1	Max	3 × 3	1	1	93.4426
	11 × 11	2	1	1	Max	3 × 3	1	1	90.1639
	13 × 13	2	1	1	Max	3 × 3	1	1	50.82
2	9 × 9	2	1	1	Max	3 × 3	1	1	93.4426
	9 × 9	4	1	1	Max	3 × 3	1	1	90.4426
	9 × 9	6	1	1	Max	3 × 3	1	1	80.56
	9 × 9	8	1	1	Max	3 × 3	1	1	75
	9 × 9	10	1	1	Max	3 × 3	1	1	80.56
	9 × 9	12	1	1	Max	3 × 3	1	1	72.22
	9 × 9	14	1	1	Max	3 × 3	1	1	75
3	9 × 9	2	5	1	Max	3 × 3	1	1	83.33
	9 × 9	2	4	1	Max	3 × 3	1	1	88.33
	9 × 9	2	3	1	Max	3 × 3	1	1	89.55
	9 × 9	2	2	1	Max	3 × 3	1	1	90.78
	9 × 9	2	1	1	Max	3 × 3	1	1	93.4426
4	9 × 9	2	1	0	Max	3 × 3	1	1	80
	9 × 9	2	1	1	Max	3 × 3	1	1	93.4426
	9 × 9	2	1	2	Max	3 × 3	1	1	83.33
	9 × 9	2	1	S	Max	3 × 3	1	1	Non
5	9 × 9	2	1	1	Max	3 × 3	1	1	93.4426
	9 × 9	2	1	1	Ave	3 × 3	1	1	88.78
6	9 × 9	2	1	1	Max	3 × 3	1	1	93.4426
	9 × 9	2	1	1	Max	5 × 5	1	1	75
	9 × 9	2	1	1	Max	7 × 7	1	1	44.2623
	9 × 9	2	1	1	Max	9 × 9	1	1	88.89
	9 × 9	2	1	1	Max	11 × 11	1	1	63.9344
	9 × 9	2	1	1	Max	13 × 13	1	1	80.56
7	9 × 9	2	1	1	Max	3 × 3	6	1	83.33
	9 × 9	2	1	1	Max	3 × 3	5	1	84
	9 × 9	2	1	1	Max	3 × 3	4	1	81.78
	9 × 9	2	1	1	Max	3 × 3	3	1	96.7213
	9 × 9	2	1	1	Max	3 × 3	2	1	86.11
	9 × 9	2	1	1	Max	3 × 3	1	1	93.4426
8	9 × 9	2	1	1	Max	3 × 3	3	0	80.56
	9 × 9	2	1	1	Max	3 × 3	3	1	96.7213
	9 × 9	2	1	1	Max	3 × 3	3	2	55.56
	9 × 9	2	1	1	Max	3 × 3	3	S	Non

- 2 bordered pixels while maintaining the same original channel size, it was found that benchmarked best %age value 93.44% for 1 bordered pixels is exactly the same.

Two forms of pooling are first examined for the pooling layer. The average (Ave.) and maximum (Max.) are these. For the Max, the best outcome of 93.44% was noted. When window size is adjusted from 3x3 to 13x13 pixels, 3x3 pixels yields the greatest performance (93.44%). When the pooling layer's stride size is changed from 1x1 pixels to 6x6 pixels, best %age value of 96.72% had measured at 3x3pixels. Both the "same" pixels and the bordered pixels are altered from 0 to 2 for the zero padding sizes. The greatest result, 96.72%, at 1 pixels has been reported.

Pooling type Max., pooling stride size equals 3×3 pixels, pooling window size equals 3×3 pixels, convolution filter size equals 9×9 pixels, pooling size equals 3 bordered pixels (each pixel includes 0 value), number of convolution filters equals 2, convolution stride size equals 1×1 pixels, as well as convolution padding size equals 1 bordered pixel. These parameters yield highest accuracy after extensive testing. For the suggested LL-DFI-Net model, these values serve as a benchmark. In the Medium Case, the following parameters show maximum accuracy: When the convolution filter size is 3x3 pixels, number of convolution filters is 10, convolution stride size was 2x2 pixels, convolution padding size is 1 bordered pixel, the pooling type Max., the pooling window size is 9x9 pixels, the pooling stride size is 4x4 pixels, and the pooling size is 1 bordered pixel (each pixel contains a zero value), the accuracy results are 97.92%. For the suggested ML-DFI-Net model, these values serve as a benchmark. In the High Case, the accuracy is 100% for the following parameters: Pooling window size is 3 x 3 pixels, pooling stride size is 1 x 1 pixels, pooling type is Max., and pooling size is 1 bordered pixels (each pixel contains 0 value). The convolution stride size is 3×3 pixels, the number of convolution filters is 2, and the convolution filter size is also 3×3 pixels. For suggested HL-DFI-Net model, these values serve as a benchmark.

4.4 Resizing Input Images

The original image size is $320 \times 240 \times 3$ this represent a big size according the options of lab-top, because that resize image in to $256 \times 256 \times 1$ and convert it to gray image to reduce the time for training.

Since $256 \times 256 \times 1$ pixels yields greatest comparative result for 3 cases, suggested DFI-net model is modified for this input size.

4.5 Training and Testing

For training phase, half of all photos in DFU dataset were arbitrary selected, and for validation phase, random selection is made from 25 percent of images included in same dataset. For testing phase, random selection of 25 percent of entire dataset's photos is employed. The testing phase evaluates suggested DFI model. FIGURE 4, shows proposed DFI network's training and validation results.

Training loss, iterations per epoch, as well as validation accuracy are primary metrics shown in these figures. The first curve illustrates correlations between iteration and percentage correctness, while second curve displays the correlations between iteration and loss/error. Accuracy may be sharply improved to maximum value while loss/error could be drastically decreased. It follows that training the suggested DFI-Net is a successful implementation.

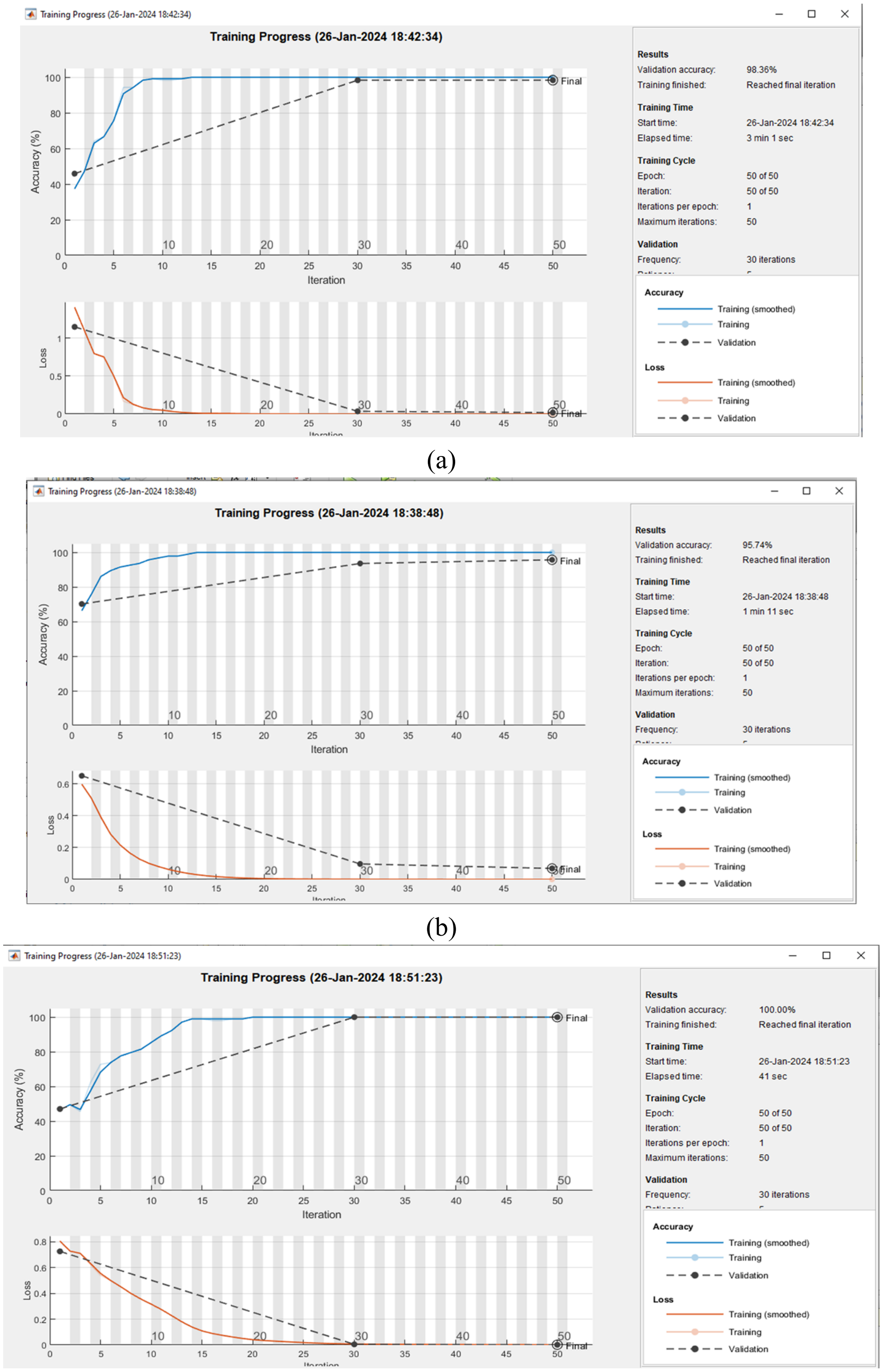

Results
Validation accuracy: 98.36%
Training finished: Reached final iteration

Training Time
Start time: 26-Jan-2024 18:42:34
Elapsed time: 3 min 1 sec

Training Cycle
Epoch: 50 of 50
Iteration: 50 of 50
Iterations per epoch: 1
Maximum iterations: 50

Validation
Frequency: 30 iterations

(a)

Results
Validation accuracy: 95.74%
Training finished: Reached final iteration

Training Time
Start time: 26-Jan-2024 18:38:48
Elapsed time: 1 min 11 sec

Training Cycle
Epoch: 50 of 50
Iteration: 50 of 50
Iterations per epoch: 1
Maximum iterations: 50

Validation
Frequency: 30 iterations

(b)

Results
Validation accuracy: 100.00%
Training finished: Reached final iteration

Training Time
Start time: 26-Jan-2024 18:51:23
Elapsed time: 41 sec

Training Cycle
Epoch: 50 of 50
Iteration: 50 of 50
Iterations per epoch: 1
Maximum iterations: 50

Validation
Frequency: 30 iterations

(c)

Figure 4: (a) Training process (accuracy and loss) for the Dataset of LL-DFI-Net, (b) Training process (accuracy and loss) for the Dataset of ML-DFI-Net. (c) Training process (accuracy and loss) for the Dataset of HL-DFI-Net.

5. CONCLUSION

To sum up, this research presents comprehensive AI-based approach for assessing diabetic foot ulcers using infrared thermography and tailored CNN models. The three networks developed—Low-Level Diabetic Foot Infection Network (LL-DFI-Net), Medium-Level Diabetic Foot Infection Network (ML-DFI-Net), and High-Level Diabetic Foot Infection Network (HL-DFI-Net)—demonstrated high accuracy in detecting different risk levels associated with diabetic foot complications. Specifically, LL-DFI-Net achieved an accuracy of 96.72%, ML-DFI-Net recorded 97.92%, and HL-DFI-Net reached 100%. These results highlight the potential of our approach to significantly improve clinical results by making earlier and more accurate interventions possible for diabetic foot disorders.

We acknowledge that the dataset's specific sources may introduce regional or demographic biases. Future research will focus on incorporating a more diverse set of data to better address these biases and enhance applicability of our findings.

References

[1] Rowley WR, Bezold C, Arikan Y, Byrne E, Krohe S. Diabetes 2030: Insights From Yesterday, Today, and Future Trends. Popul Health Manag. 2017;20:6-12.

[2] Gaussorgues G, Chomet S. Infrared Thermography.Springer Science Business Media; 2012;5.

[3] Lawson L, Bridges EJ, Ballou I, Eraker R, Greco S, et al. Accuracy and Precision of Noninvasive Temperature Measurement in Adult Intensive Care Patients. Am J Crit Care. 2007;16:485-496.

[4] Mahajan P, Madhe S. Hypo and Hyperthyroid Disorder Detection From Thermal Images Using Bayesian Classifier. In: International Conference on Advances in Communication and Computing Technologies (ICACACT 2014). IEEE PUBLICATIONS;2014; 2014:1-4.

[5] Capo A, Ismail E, Cardone D, Celletti E, Auriemma M, et al. Joint Functional Impairment and Thermal Alterations in Patients With Psoriatic Arthritis: A Thermal Imaging Study. Microvasc Res. 2015;102:86-91.

[6] Frykberg RG, Gordon IL, Reyzelman AM, Cazzell SM, Fitzgerald RH, et al. Feasibility and Efficacy of a Smart Mat Technology to Predict Development of Diabetic Plantar Ulcers. Diabetes Care. 2017;40:973-980.

[7] Ammer K. Medical Thermology 2017-a Computer-Assisted Literature Survey. Thermol Int. 2018;28.

[8] Pine A, Novice T, Vanwieren B, Wagner C, Schmidt BM, et al . Liquid Crystal Thermochromic Technology to Prevent Diabetic Foot Ulcers. Diabet Foot. 2021;24:45.

[9] Noor S, Raghav A, Parwez I, Ozair M, Ahmad J. Molecular and Culture Based Assessment of Bacterial Pathogens in Subjects With Diabetic Foot Ulcer. Diabetes Metab Syndr. 2018;12:417-421.

[10] Ming A, Walter I, Alhajjar A, Leuckert M, Mertens PR. Study Protocol for a Randomized Controlled Trial to Test for Preventive Effects of Diabetic Foot Ulceration by Telemedicine That Includes Sensor-Equipped Insoles Combined With Photo Documentation. Trials. 2019;20:521.

[11] Lahiri BB, Bagavathiappan S, Philip J. Infrared Thermal Imaging Based Study of Localized Cold Stress Induced Thermoregulation in Lower Limbs: The Role of Age on the Inversion Time. J Therm Biol. 2020;94:102781.

[12] Koerner S, Adams D, Harper SL, Black JM, Langemo DK. Use of Thermal Imaging to Identify Deep-Tissue Pressure Injury on Admission Reduces Clinical and Financial Burdens of Hospital-Acquired Pressure Injuries. Adv Skin Wound Care. 2019;32:312-320.

[13] Ramirez-GarciaLuna JL, Bartlett R, Arriaga-Caballero JE, Fraser RD, Saiko G. Infrared Thermography in Wound Care, Surgery, and Sports Medicine: A Review. Front Physiol. 2022;13:838528.

[14] van Netten JJ, van Baal JG, Liu C, van Der Heijden F, Bus SA. Infrared Thermal Imaging for Automated Detection of Diabetic Foot Complications. J Diabetes Sci Technol. 2013;7:1122-1129.

[15] Khandakar A, Chowdhury ME, Reaz MB, Ali SH, Kiranyaz S, et al. A Novel Machine Learning Approach for Severity Classification of Diabetic Foot Complications Using Thermogram Images. Sensors. 2022;22:4249.

[16] Abdel-Jaber H, Devassy D, Al Salam A, Hidaytallah L, EL-Amir M. A Review of Deep Learning Algorithms and Their Applications in Healthcare. Algorithms. 2022;15:71.

[17] Janssens O, Van de Walle R, Loccufier M, Van Hoecke S. Deep Learning for Infrared Thermal Image Based Machine Health Monitoring. IEEE ASME Trans Mechatron. 2017;23:151-159.

[18] Batchuluun G, Lee YW, Nguyen DT, Pham TD, Park KR. Thermal Image Reconstruction Using Deep Learning. IEEE Access. 2020;8:126839-126858.

[19] Nguyen AD, Choi S, Kim W, Ahn S, Kim J et.al . Distribution Padding in Convolutional Neural Networks. In: Ieee International Conference on Image Processing(ICIP). IEEE PUBLICATIONS. 2019;2019:4275-4279.

[20] Ide H, Kurita T. Improvement of Learning for CNN With Relu Activation by Sparse Regularization. In: 2017 International Joint Conference on Neural Networks (IJCNN). IEEE PUBLICATIONS; 2017:2684-2691.

[21] Brownlee J. A Gentle Introduction to Pooling Layers for Convolutional Neural Networks. Com/Pooling-Layers-For-Convolutional-Neural-Networks. Accessed,. 2019;4:2021.

[22] “Minus 40°C to 300°C, Thermal Imager Infrared Camera,8HZ, Digital Handheld Thermal Imaging Devices, 2.8in LCD Screen Digital Handheld Multifunctional Thermal Imager: : Industrial & Scientific,” Amazon.

[23] Al-Nima RR, Al-Hatab MM, Qasim MA. An Artificial Intelligence Approach for Verifying Persons by Employing the Deoxyribonucleic Acid (Dna) Nucleotides. J Electr Comput Eng. 2023;2023:6678837.

[24] Al-Hatab MM, Al-Obaidi AS, Al-Hashim MA. Exploring Cie Lab Color Characteristics for Skin Lesion Images Detection: A Novel Image Analysis Methodology Incorporating Color-Based Segmentation and Luminosity Analysis.2024;15:88-97.

[25] Fathel WR, Al-Obaidi AS, Qasim MA, Al-Hatab MM. Skin Cancer Detection Using K-Means Clustering-Based Color Segmentation. Texas J Eng Technol. 2023;18:46-52.

[26] Al-Hatab MM, AlNima MZ. Hematological Classification of White Blood Cells by Exploiting Digital Microscopic Images.Eurasian Res. Bull. 2023;18:44-52.